Design considerations for an underwater soft-robot inspired from marine invertebrates

Bioinspiration & Biomimetics

Design considerations for an underwater soft-robot inspired from marine invertebrates

Michael Krieg[1,3], **Isaac Sledge**[2,3] **and Kamran Mohseni**[1,2,3]

1   Department of Mechanical and Aerospace Engineering, University of Florida, USA
2   Department of Electrical and Computer Engineering, University of Florida, USA
3   Institute for Networked Autonomous Systems, University of Florida, USA

E-mail: mohseni@ufl.edu

Abstract

This article serves as an overview of the unique challenges and opportunities made possible by a soft, jellyfish inspired, underwater robot. We include a description of internal pressure modeling as it relates to propulsive performance, leading to a desired energy-minimizing volume flux program. Strategies for determining optimal actuator placement derived from biological body motions are presented. In addition a feedback mechanism inspired by the epidermal line sensory system of cephalopods is presented, whereby internal pressure distribution can be used to determine pertinent deformation parameters.

1. Introduction

The field of soft robotics has received much attention lately. One reason is that rigid structures are prone to critical failure when disturbances or perturbations result in high enough stress; whereas, soft structures are capable of bending to accommodate the disturbance and return to an operational state [53]. In addition, there are several situations, such as tactile sensing or grasping where flexibility in an actuator can prove advantageous to a desired action. This is often the case in biological underwater locomotion [32], but generally not reflected in propeller-dominated underwater robotics.

Flexibility is a defining property of propulsion in marine animals [31]. Fine musculature and compliant membranes permit both active and passive control of swimming appendages. The degree of flexibility exhibited in propulsive mechanisms varies widely across marine animals. The flexibility ranges from thunniform swimmers, which can be generalized as conjoined rigid elements, to invertebrates like jellyfish containing no rigid elements whatsoever. One common element seems to be that flexibility in flapping foils enhances propulsive output, propulsive efficiency, or both [32, 59–61].

Marine mammals and fish utilize an inner rigid skeletal structure with muscles, tendons, and flexible membranes layered on top. Thunniform swimmers, which are mostly rigid with oscillatory bending in the caudal fin, can be replicated by a series of joints and rigid tail sections creating the biological kinematics without specifically incorporating flexible materials [3, 5, 58]. During testing on these platforms, it is observed that the body deformations significantly reduce the drag of the vehicle compared to a completely rigid hull [5]. This represents a form of flexibility which is actively controlled with no freedom of motion. Pectoral fin paddling in labriform swimming, on the other hand, employs passive flexibility via flexible rays running down the fins [16, 28]. This flexibility actually allows the fin to generate maneuvering forces in the desired direction, whether the fin is flapping in towards the body or out away from it, a feature which is present in passively flexible biomimetic fins [51], but not rigid ones [18]. Many experimental studies have looked into the advantages of flexible flapping foils in terms of thrust production [1, 15, 52] and power input [13]. Quinn *et al* [42] investigated the effects of multiple, self-propelled swimming bodies, showing an increase in propulsive economy with higher flexibility and slower swimming speeds.

Other marine animal swimming modes like anguilliform and rajiform require large scale undulations. Even though the deformation of the overall body shape is actively controlled, external flexible membranes become necessary to maintain the body shape, and thus play some role in the propulsive mechanisms.
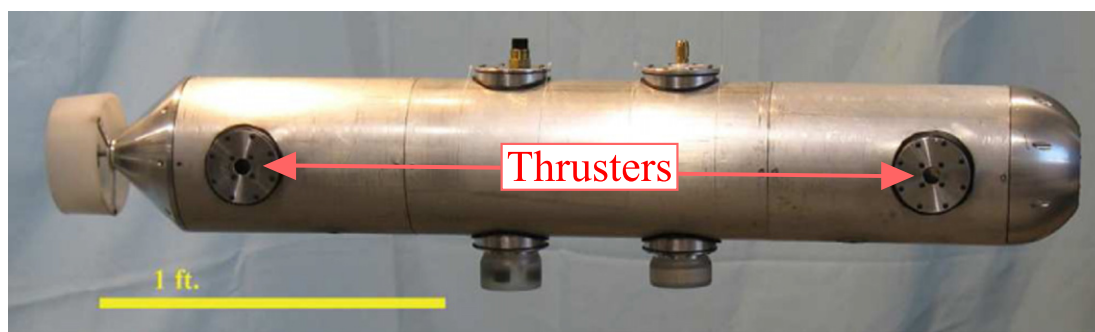
Figure 1. Traditional rigid underwater robot utilizing cephalopod inspired thrusters. For more information on this vehicle refer to [19].

Clark and Smits fabricated an actively oscillating, deformable fin, derived from manta rays, and analyzed its hydrodynamic properties [11]. Additional studies were carried out by Moored *et al* [36] to assess its swimming potential and efficiency. Further progress is highlighted in the survey article of Moored *et al* [37].

So far, all the examples we have highlighted can be adapted to standard robotic platforms relatively easily, in that the flexibility exists in the propulsor, and the robot itself, or internal structure, is still a rigid body to which motors and standard actuators can be affixed. It is in this regard that marine invertebrates, specifically those belonging to phylum *Medusozoa* and class *Cephalopoda*, are unique. These marine animals have no rigid internal structures and maintain desired shape utilizing what is referred to as a 'muscular hydrostat'. In a 'muscular hydrostat' arrangement, muscles not only drive body motions, but also provide skeletal support for those motions. As such, these animals provide a biological model to help guide designs of a completely soft robot, absent of any rigid structures. One common feature to the locomotion of these marine invertebrates is the periodic generation of finite propulsive jets. Much like synthetic jet actuators used for flow control, these animals alternate between ingesting and expelling fluid so that there is no net mass flux over an entire cycle, but there is a positive momentum flux providing propulsion. As an example, consider jellyfish body deformations used to generate the propulsive jets, which are shown for distinct time segments of *Sarsia tubulosa* swimming later in figure 6. This propulsion mechanism begins when the jellyfish body contracts which reduces the sub-umbrellar cavity volume and forces out a propulsive jet. Immediately after that the body expands back to its former volume refilling the cavity. After a period of coasting, the pulsation cycle is complete and the jellyfish starts a new cycle.

The vortex ring formation associated with pulsed jets is known to enhance the impulse transfer compared to continuous jets with equivalent volume flux [27] due to a converging radial velocity induced by the forming vortex ring [23]. This type of propulsion has

been utilized to provide accurate low speed maneuvering to slender, low drag, underwater robots [19–21, 35]. Since the thruster can be placed just inside the vehicle hull, the streamlined hull shape is unaffected by adding thrusters for maneuvering, as can be seen in figure 1. Pulsed-jets have also been used as the primary means of propulsion, demonstrating a higher propulsive efficiency than previously assumed for high momentum jet propulsion [38, 39], much like squid themselves [6, 7]. Although the thrusters draw inspiration from the propulsion of squid and jellyfish, they have generally been used on traditional rigid underwater vehicles. Clearly the morphology of these animals indicates that this type of propulsion could easily be applied to underwater soft robotics. Some soft robots inspired by this type of propulsion include a jellyfish shaped robot employing shape memory alloy composite actuators to drive bell contraction [55, 56], and a soft robot was created by casting a mold from the mantle of *Octopus vulgaris* that expelled jets by mimicking the radial contraction of the mantle [48]. In addition the fiber support structure in squid mantles can also be used as inspiration for soft robot body design. The interwoven tunic fiber structures help maintain the shape of the squid and distribute the action of the muscles [17, 34, 57]. Furthermore, their alignment maximizes both the propulsive output for a given contraction and the energy storage in fibers released during mantle re-inflation [22]. A similar support structure could greatly reduce the number of required actuators in a soft robot, reducing its complexity.

In this paper we examine the functional requirements of a soft robot with no rigid parts, utilizing not only the propulsion mechanisms of cephalopods and jellyfish, but also aspects of their musculature, morphology, and sensory mechanisms for inspiration in the design and control strategy. This discussion begins with a brief overview of the thrust and pressure dynamics inside flexible jetting cavities, which identifies energy optimal volume flux programs in section 2. In section 3, methods for determining the best locations of body deformation actuators from biological

models are presented. Finally, we make it possible to close the control loop, in section 4, by introducing a bioinspired sensory feedback mechanism capable of determining body deformation parameters from pressure distributions.

2. Pressure dynamics and minimal work

When squid and jellyfish eject jets to propel themselves through the water, they create an imbalance between the pressure of the internal cavity and the pressure of the external fluid, which drives locomotion. Therefore, the internal pressure dynamics are of vital importance when designing a soft underwater robot inspired by this type of propulsion. The external pressure distribution also strongly affects the swimming of these animals; however, the dynamics associated with the external pressure distribution are fundamentally different than those for the internal pressure. The external pressure forces on moving underwater bodies are generally categorized as drag or added mass forces and there are multiple studies focusing on reducing these forces. The analysis of this section does not consider the effect of body deformation on external pressure, but rather focuses on how body deformations can minimize total work required for propulsive jetting. However, these deformations are likely still optimal when taking into account external pressure forces as well, given that small scale deformations required for jetting will have very little effect on the overall drag profile. Also, during jetting the jetting forces themselves are much stronger than the drag forces, as evidenced by the massive accelerations of these animals.

A model for the internal pressure distribution of any axisymmetric deformable cavity body is provided in [24]. The model allows us to relate the internal pressure to the deformation of the cavity, which is what will be directly controlled by the proposed soft robot. In that study, it was shown that there is a direct link between the pressure inside of a jetting cavity and the total circulation dynamics of the system:

$$P_b = \frac{d\Gamma_{\text{Jet}}}{dt} + \frac{d\tilde{\Gamma}_{\text{Cav}}}{dt} - \frac{1}{2}u_b^2. \quad (1)$$

In this equation, P_b is a reference pressure at the intersection of the inner cavity surface and the axis of symmetry, u_b is the velocity of the surface at that point, Γ_{Jet} is the circulation of the entire region downstream of the cavity opening (which we refer to as the jet region for simplicity), and $\tilde{\Gamma}_{\text{Cav}}$ is the circulation within the cavity not including the circulation terms specifically due to stretching boundaries.

The usefulness of such modeling lies in the fact that circulation is an invariant of motion for inviscid flows, and thus the rate of change of circulation in either cavity or jet region can be calculated as a sum of vorticity flux and source terms. The simplest case to describe is when the cavity body is ejecting a

propulsive jet starting from rest. Subsequent jetting cycles involve interactions between incoming fluid vortex structures and the internal boundaries, as described by the impingement circulation terms in [24]. As a first step, this paper will discuss control algorithms for a soft jetting robot during this first jetting cycle to illuminate the control strategy before moving on to the more complex cases.

For this case, there are only two sources of circulation. The emanating fluid carries with it a shear layer created on the surface of the nozzle opening. This can be considered a flux of vorticity into the jet region. The rate at which vorticity is expelled into the jet region scales with the jet velocity squared. Inside the cavity there is a circulation due to the fluid which converges towards the thruster opening. The flow on the inside of the opening can be modeled as a half-sink of finite circular area [24]. The circulation of the internal flow scales with the volume flux (strength of the sink), so that the rate of change of internal circulation scales with jet acceleration. Therefore, for this simplified case, the reference pressure on the inside of the cavity can be calculated as

$$P_b = C_1 \dot{\Omega}^2 + C_2 \ddot{\Omega} + \frac{1}{2}u_b^2, \quad (2)$$

where $\dot{\Omega}$ is the volume flux crossing the opening, $\ddot{\Omega}$ is the rate of change of the volume flux, and C_1 and C_2 are constants which mostly depend on nozzle geometry and can be determined from [23] and [24], respectively. For most cases, the cavity surface velocity u_b is very small compared to jet velocity and this term can be neglected making the reference pressure a function only of volume flux and its time derivative. This relationship between pressure and volume flux parameters (through generation of circulation) was verified in [24] using a prototype bioinspired jet thruster very similar to ones placed on rigid vehicles depicted in figure 2. The prototype jet thrusters expel fluid by moving a semi-flexible mechanism, which is reinforced with a helical spring so that it maintains a consistent diameter and has a linear relationship between plunger deflection and volume flux. As is summarized in figure 3, the pressure predicted by (2) compared to the pressure measured on the plunger surface shows high accuracy, and is discussed in greater detail in [24] for different volume flux programs.

This form of jet propulsion is inherently unsteady, as the jet flow must be terminated in between pulsation cycles to allow for refilling; which contrasts with continuous jet propulsion commonly used in recreational watercraft (jetskis, bow thrusters, etc). Therefore, it is important to know if certain volume flux programs are beneficial to propulsion, or more specifically to propulsive efficiency, and design the robot controller accordingly. The total power which must be delivered to drive fluid motion for any general cavity shape and deformation was defined in [24] as the product of local pressure and cavity surface boundary
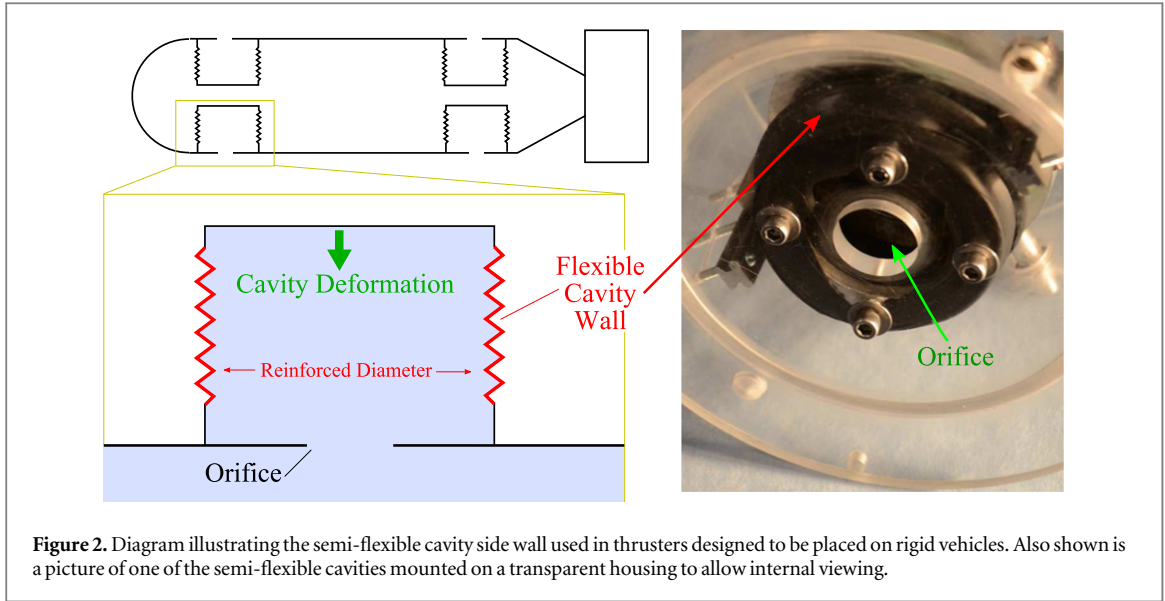
Figure 2. Diagram illustrating the semi-flexible cavity side wall used in thrusters designed to be placed on rigid vehicles. Also shown is a picture of one of the semi-flexible cavities mounted on a transparent housing to allow internal viewing.
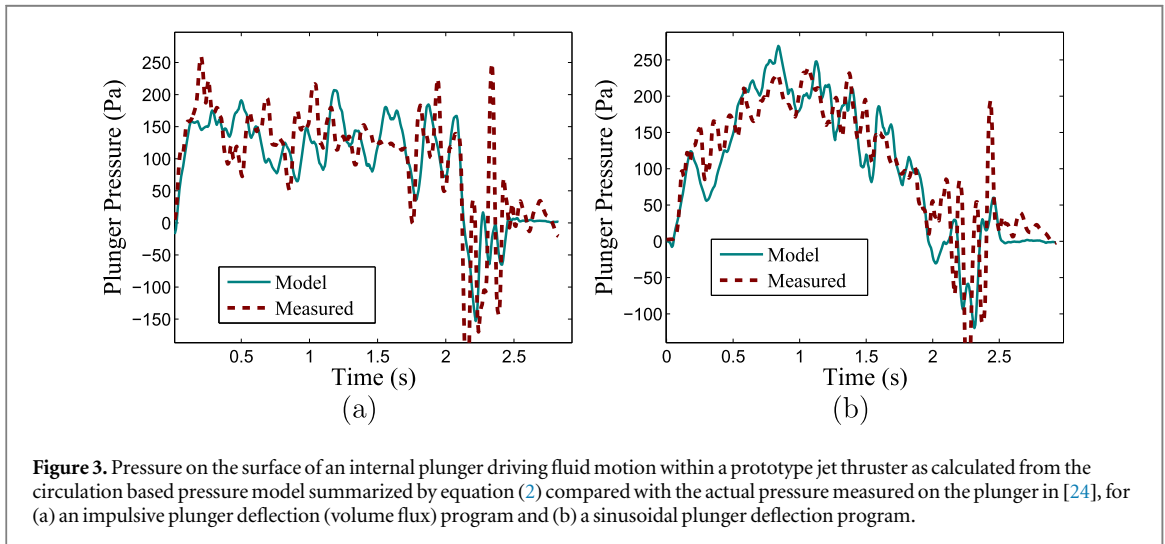

Figure 3. Pressure on the surface of an internal plunger driving fluid motion within a prototype jet thruster as calculated from the circulation based pressure model summarized by equation (2) compared with the actual pressure measured on the plunger in [24], for (a) an impulsive plunger deflection (volume flux) program and (b) a sinusoidal plunger deflection program.
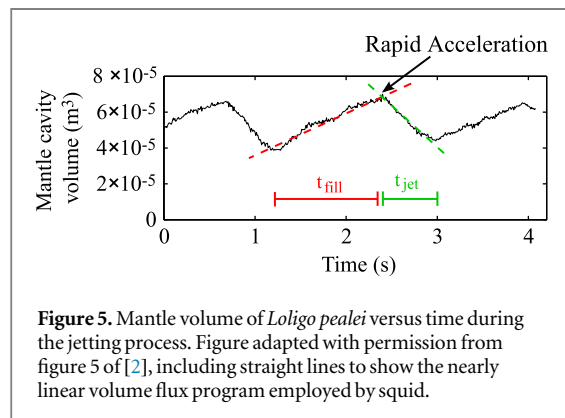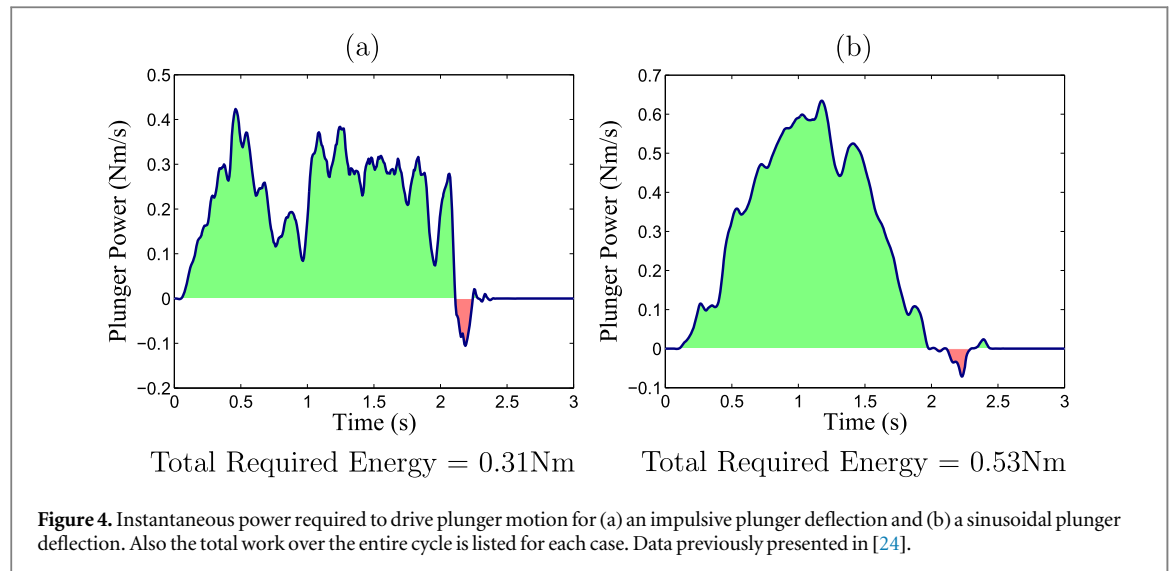
velocity integrated over the entire surface

$$\frac{dW}{dt} = 2\pi \int_{\sigma} r_{\sigma} P \vec{u}_{\sigma} \cdot \hat{n} \, ds, \tag{3}$$

where W is the total work required for jetting, σ is the cavity surface boundary, P is the pressure at any location s along the boundary surface, r_{σ} is the radial coordinate at s, $\hat{n}$ is the normal unit vector at s, and $\vec{u}_{\sigma}$ is the velocity of the surface at s due to deformation. The geometry of the jetting cavity and controlled deformations dictate the values for σ, $\vec{u}_{\sigma}$, and $\hat{n}$; whereas the local pressure distribution $P(s)$ must be calculated. One method to calculate the pressure distribution by integrating the momentum equation along a strategic viscosity free path is described in [24]. The integral of (3) cannot be reduced for any general cavity shape, but often the specific cavity geometry will allow pressure and work terms to be greatly simplified. For the specific prototype actuator geometry in [24], the pressure is uniform over the internal plunger plate, and the total work is just the product of the reference pressure, P_b, the area of the plunger, and the velocity of the plunger. It was determined in that study that an impulsive volume flux program requires less energy than a smoother sinusoidal program with equivalent momentum transfer. The power required to drive fluid motion is shown over the entire program for two such cases in figure 4, including the total work required for each program. The energetic advantage of the impulsive deflection program exists because the peaks in boundary deformation velocity and pressure force are out of phase for the impulsive program and coincident for the sinusoidal program. Since the power required to drive the submerged surface is the product of the boundary velocity and the pressure at its surface, which it must act against, it is advantageous to have a low boundary velocity when the pressure is high, and similarly a high boundary velocity when the pressure is lower.

As can be inferred from the form of (3), the total work required for propulsion will change slightly with different flexible cavity geometries. However, the

Figure 4. Instantaneous power required to drive plunger motion for (a) an impulsive plunger deflection and (b) a sinusoidal plunger deflection. Also the total work over the entire cycle is listed for each case. Data previously presented in [24].

Figure 5. Mantle volume of *Loligo pealei* versus time during the jetting process. Figure adapted with permission from figure 5 of [2], including straight lines to show the nearly linear volume flux program employed by squid.

swimming behavior of the squid *Loligo pealei* suggest that the impulsive volume flux program is actually beneficial for a much larger range of cavity geometries. The squid mantle volume program reported in [2] is reproduced here in figure 5 to show the nearly constant volume flux during jetting and refilling, and significant accelerations when switching back and forth. It should be noted that, in contrast to the prototype actuator in [24] which generated volume changes with an axially deflecting internal plunger, the squid generates volume change by deforming the mantle surface radially (circumferential muscle contraction). Therefore, the energetic benefit of offsetting peaks in internal pressure and deformation velocity by utilizing an impulsive flux program are apparently independent of the specific deformation geometry.

A volume flux program which reduces the total energy required for propulsion is likewise desirable in the kinematics of soft jetting robots. The discussion of this section indicated that an impulsive velocity program will decrease total required energy for propulsion, but the optimal program will likely have some variations with body geometry. In the following sections, we will discuss deformation of a soft robot with a specific jellyfish-like geometry, including a general algorithm for determining actuator placement on bioinspired robots, and introduce a feedback mechanism inspired by cephalopod epidermal line sensing to maintain a given desired jetting program. In addition, though not discussed in this paper specifically, epidermal-line-inspired sensors have also been used as a mechanism for determining exact external hydrodynamic forces. These forces can be used as a feed-forward mechanism to improve vehicle controller stability [62].

3. Placement of soft-body actuators

The previous section discussed pressure generation inside jetting cavities, and presented volume flux patterns which minimize the total work required for propulsion. That analysis was based on circulation generating mechanisms, without specific consideration for the geometry of the cavity or how the cavity is deformed to generate the desired volume flux. In this section, we discuss possible cavity geometries with varying degrees of flexibility and actuation techniques; recognizing that biological morphology has evolved to simultaneously optimize multiple objectives, we introduce a method for automatically selecting actuator locations from recorded body deformations.

Biologically inspired pulsed jet thrusters require at least some degree of flexibility in order to deform the thruster cavity and drive the volume flux. The thrusters placed on rigid vehicles have a flexible cavity side wall [19, 20], as illustrated in figure 2. Since the mostly rigid thrusters are reinforced in such a way that the deformation is limited to a single parameter, there is a unique deformation program for any desired volume flux. This means that in order to create a desired impulsive velocity program, the thruster must perform an impulsive cavity top plate deflection.

If this propulsive technology is to be applied to a soft robotic platform, it is more difficult to restrict the

Table 1. A summary of the geometry, physical, and flow characteristics for motion primitives of *Sarsia tubulosa*, as determined in [50].

Phase	Geometry/Physical change	Effects on flow
Pressurize	There is an outward rotation of the velar flap and a pressurization of the subumbrellar cavity. Half-sink terms dominate.	The outward flow across the velum increases sharply.
Jetting (Acceleration)	The bell compresses and the velar flap continues to rotate outward. An increase in pressure is seen due to vorticity flux. The power is maximized.	An ejecting jet is formed. Part of the fluid slug is ejected in this phase.
Jetting (Deceleration)	The minimum velar diameter and bell volume are achieved. The maximum bell pressure and upstream thrust are achieved.	Propulsive vortex ring formation, separation, and translation occurs. The remainder of the slug is moved into the ring before separation.
Refill	The cavity volume and velar diameter increase. An upstream thrust is generated due to the relaxation vortex striking the cavity.	There is an inward flow of fluid, which refills the subumbrellar cavity. A relaxation vortex is also formed inside the cavity.
Coasting	There are slight velar oscillations due to small pressure changes.	There are slight inward and outward flow changes across the velum. The relaxation vortex diffuses.

cavity deformation to a single parameter. Furthermore, a specific optimal body shape and body shape deformation for a soft jetting robot are ambiguous, making the restrictions on body shape and deformation similarly nebulous. However, marine invertebrates have had eons to develop desirable flexible body shapes (jellyfish especially, being one of the oldest living animals on the planet). In this section, we use the morphology of jellyfish, specifically *Sarsia tubulosa*, as a hypothetical basis for body shape, and to determine a minimum number and location of actuators required for deformation of this body. Although this process is done for a specific species of jellyfish (and its exact body shape), because of available data on body motions and pressure dynamics of that species, it could easily be applied to the body motions of any other marine invertebrate.
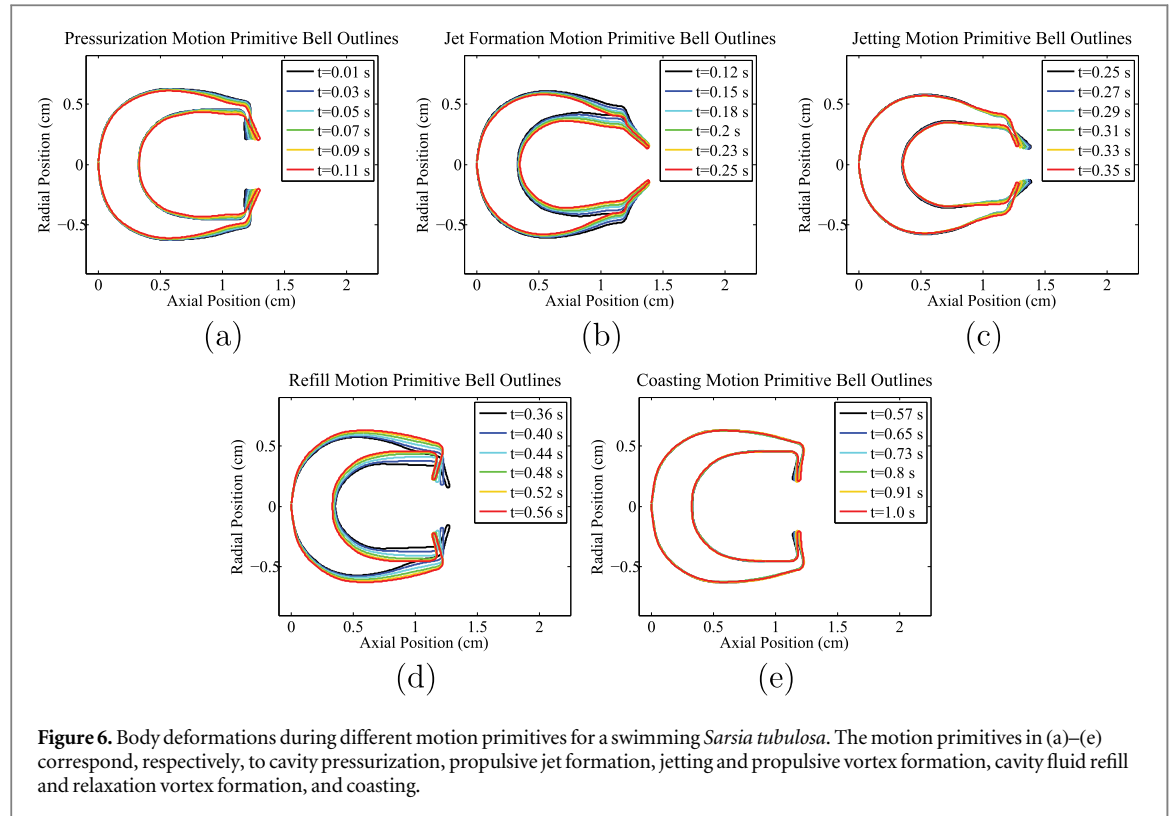
We can find reasonable configurations of actuators by leveraging a dynamical-systems-based model that we introduced in [50]. This process was originally designed to uncover motion primitives, which are subsets of kinematics sequences from some entity that contains variable-duration actions. However, since the algorithm also characterizes both the kinematics and change in kinematics, insight as to where prominent changes occur in an entity's body during a motion sequence can also be drawn. From these insights we conclude the necessary number and locations of actuators needed to drive the motion. We will first introduce the algorithm developed to segment complex body motions into motion primitives from [50], and brief descriptions of the motion primitives determined for a *Sarsia tubulosa* swimming cycle, before deriving analysis on how the expectation of stochastic systems can be leveraged to define suitable actuator locations for this study.

The motion primitive analysis given in [50] characterizes body deformations as an aggregation of stochastic differential equations, which capture the average spatial and temporal evolution of body kinematics. The stochastic ODEs take the form: $\mathrm{d}y_k^m$

$(t; p) = -a_k^m(y_k^m(t; p) - b_k^m)\mathrm{d}t + \sum_i \kappa_{i,k}^m(t)^{1/2}$ $\mathrm{d}B_k^m(t)$, where $\kappa_{i,k}^m(t)^2$ are draws from a Lévy-driven Gauss–Markov process at time t, B_k^m is a realization of a Brownian motion, the variables k and m are indices representing different datasets and data modalities, respectively, each differential equation is denoted by p, the average spatial behavior is dictated by b_k^m, and the average temporal behavior is governed by a_k^m. The body kinematics vector $x_k^m(t)$ is defined at each time t as: $x_k^m(t) = \sum_p w_k^m P_k^m y_k^m(t; p) + \sigma_k^m(t)$, where P_k^m is a projection matrix weighted by w_k^m and $\sigma_k^m(t)$ is a random noise term. We included a nonparametric superposition of Gauss–Markov processes [8] in the model to handle deviations from the average dynamics behavior. The Gauss–Markov processes also help to characterize rapid jumps in dynamics due to quick maneuvers. Given a kinematics sequence, we uncover the most likely parameters that could have generated the sequence using batch statistical inference [44]. Once the motion has been quantified it is segmented into primitives by temporal breakpoints associated with gradual or abrupt changes in body kinematics (for more details refer to [50]).

Body motions of *Sarsia tubulosa* were captured digitally and imported into a Navier–Stokes solver with an arbitrary Lagrangian–Eularian method [45, 46]. Lipinski and Mohseni [33] examined the flow field in and around the jellyfish with respect to material transport barriers and jellyfish feeding. When a locomotion sequence of *Sarsia tubulosa* gathered in those studies was analyzed using the segmentation algorithm discussed here, we uncovered five motion primitives in each pulsation cycle. Detailed analyses of the body dynamics and resulting flow field for each motion primitive are provided in [50].

A summary of the geometric, physical, and flow characteristics associated with each motion primitive is given in table 1, and the body motions associated with each primitive are depicted in figure 6. Despite the fact that the algorithm receives no information

Figure 6. Body deformations during different motion primitives for a swimming *Sarsia tubulosa*. The motion primitives in (a)–(e) correspond, respectively, to cavity pressurization, propulsive jet formation, jetting and propulsive vortex formation, cavity fluid refill and relaxation vortex formation, and coasting.

about the surrounding flow field, the kinematic segmentation still corresponds to stages of motion with contrasting circulation generating mechanisms. The first primitive corresponds to an outward swinging of the velar flap, due to cavity pressurization, which causes it to protrude in the downstream direction (see figure 6(a)). With a low volume flux, but substantial rate of change in volume flux (increasing) the cavity circulation is dominated by half-sink components, which drives pressurization.

The second primitive, figure 6(b), and third primitive, figure 6(c), constitute the jetting phase of the swimming cycle. During the second primitive, since both $\dot{\Omega}$ and $\ddot{\Omega}$ are positive, the vorticity flux and half-sink components work in conjunction to increase the internal pressure of the cavity generating a high propulsive force. The third primitive marks when the volume flux begins to decrease and the contribution to total circulation from the half-sink components opposes the contributions from vorticity flux ($\dot{\Omega}$ is positive, while $\ddot{\Omega}$ is negative). As such, the internal pressure reaches a maximum at the transition between the second and third primitives. Toward the end of the third primitive, the reduced volume flux greatly reduces contributions from these components. The half-sink components eventually become dominant, resulting in the negative pressure force at the end of this primitive, despite the continued jet flow.
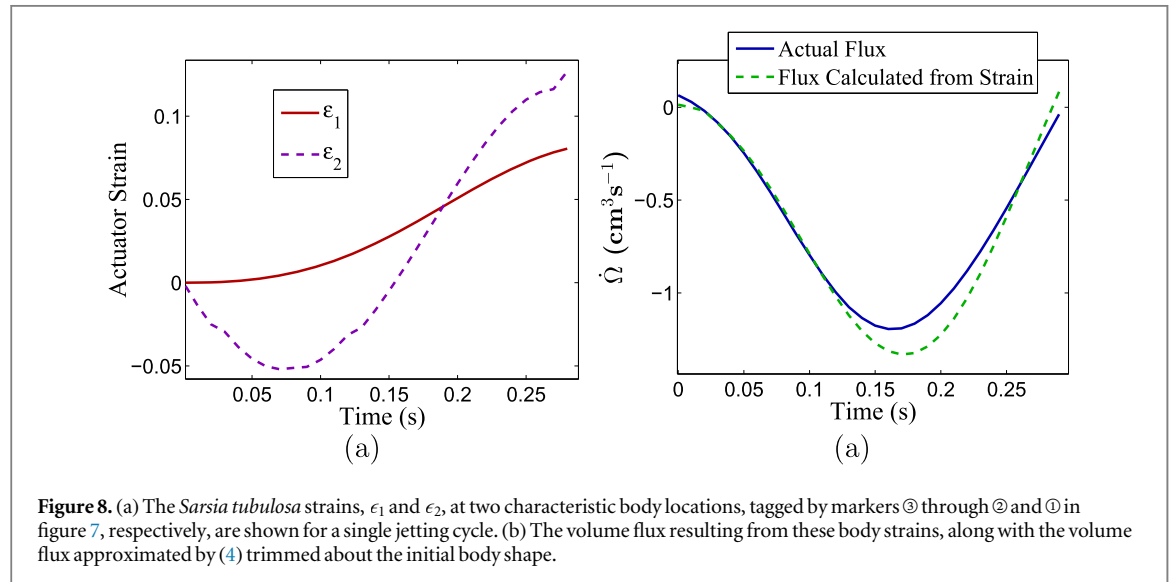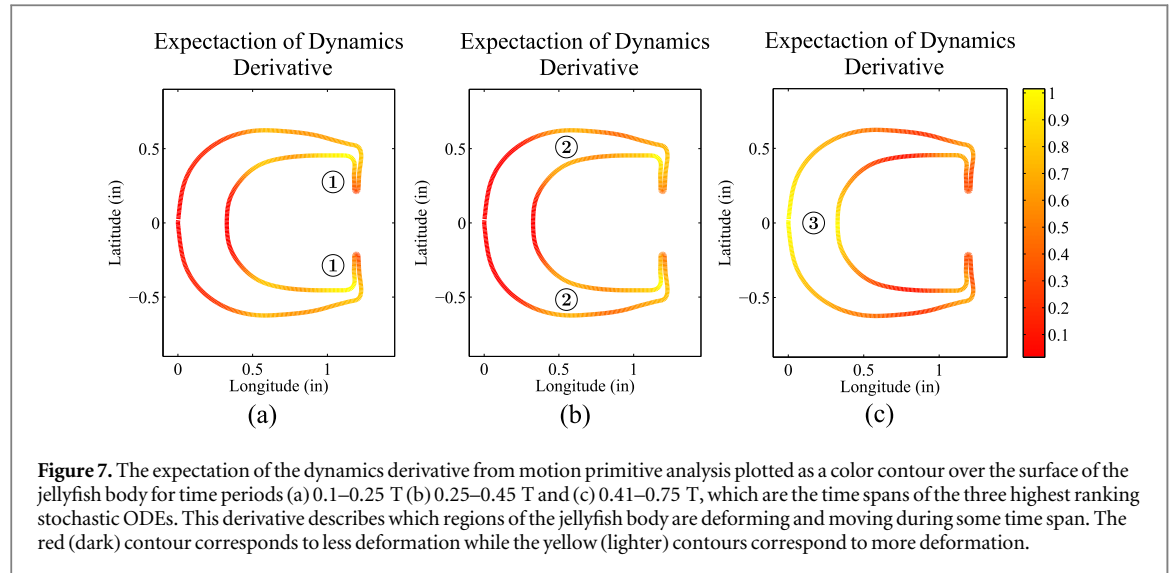
The remaining two primitives correspond to cavity fluid refill, figure 6(d), and coasting, figure 6(e). During the fourth primitive, elastic strain energy is released, causing the bell to expand. The rapid

expansion of the bell quickly draws fluid into the sub-umbrellar region, generating a relaxation vortex within the cavity. Due to the interaction of the incoming fluid with the cavity boundaries, the circulation dynamics become quite complex. For the last primitive, the only observed motions are small oscillations in the velar flap.

In addition to segmenting body motion into primitives, the set of parameters in the stochastic differential equations, which correctly quantify the motion, can also be used to establish candidate positions for actuators. This is done by first determining where there are large-magnitude deformations in the jellyfish's body, and then determining where the deformations occur for each instance.

For the first part of this procedure, we identify rapidly fluctuating stochastic differential equations associated with fast-paced, large deformations. The various differential equations are ranked according the number of Gauss–Markov processes $\kappa_{i,k}^{m}$ associated with each differential equation solution $y_{k}^{m}(t; p)$, which indicates a sudden change or divergence of body motion from the mean behavior. We then select the equations with the most Gauss–Markov processes to represent large scale changes. Since each differential equation is associated with a particular time span, we therefore know when the body is undergoing substantial changes.

The regions in which those changes occur can be discerned by analyzing the expectation, $\mathrm{d}y_{k}^{m}(t; p)$, of selected stochastic differential equations. The expectation of this dynamics derivative provides a spatially

Figure 7. The expectation of the dynamics derivative from motion primitive analysis plotted as a color contour over the surface of the jellyfish body for time periods (a) 0.1–0.25 T (b) 0.25–0.45 T and (c) 0.41–0.75 T, which are the time spans of the three highest ranking stochastic ODEs. This derivative describes which regions of the jellyfish body are deforming and moving during some time span. The red (dark) contour corresponds to less deformation while the yellow (lighter) contours correspond to more deformation.

Figure 8. (a) The *Sarsia tubulosa* strains, ϵ_1 and ϵ_2, at two characteristic body locations, tagged by markers ③ through ② and ① in figure 7, respectively, are shown for a single jetting cycle. (b) The volume flux resulting from these body strains, along with the volume flux approximated by (4) trimmed about the initial body shape.

averaged view of where and by how much the jellyfish's body changes shape. The number of modes of the dynamics derivative offers an estimate for the number of regions that change throughout the body, and hence a possible number of actuators. The relationship between the kinematics vector, $x_k^m(t)$, and the stochastic differential equation solution, $y_k^m(t; p)$, is used to map the expected values of $\mathrm{d}y_k^m(t; p)$ to the surface of the body. From our observations, the locations of the derivative modes correspond with joint-like areas.

The expectation of the three highest ranking stochastic differential equations describing the motion of *Sarsia tubulosa* are shown in figure 7. In this figure, the expected value is plotted as a color contour on the surface of the jellyfish body with yellow (lighter shade) corresponding to high amounts of deformation while red (darker) corresponds to little shape change. It can be observed that the largest shape change occurs in three regions labeled by the markers in figure 7. The

volume flux is the result of a compression of the bell which is driven by a hinge-like flapping at the location marked by ③ in figure 7(c) and an expansion at the location marked by ②. The velar flap also swings outward changing the nozzle geometry and opening diameter during jetting, using a hinge-like mechanism at the corner marked by ①.

Animal body deformations are driven by muscle contractions which will, due to conservation of volume, result in either thinning or thickening of the body. The contraction of the jellyfish bell, which drives jet expulsion, is accomplished by contraction of circumferential muscles resulting in thickening of the body at locations marked by ② and ③ in figure 7. This contraction can be accomplished with a single actuator on the soft-robot platform stretching from the axis of symmetry to the marker ②, which will be parameterized by a thickness strain in this region ϵ_1. The motion of the velar flap is correlated to oscillations in thickness of a region at the end of the bell just before the velar flap itself, marked by ① in figure 7. Even

though neuromuscular data [47] suggests that the motion of the velar flap is a passive action, we will add an additional actuator in this region to give the soft-robot full control authority, denoting the strain of this region by ϵ_2. Electro-active polymer actuators would be a good choice for the actuators on the soft robot, given the compression/expansion style of actuation as well as the required flexibility of the body. The strains in these body regions over an entire swimming cycle for *Sarsia tubulosa* are shown in figure 8(a). Next we discuss how these actuators should be operated to enact the desired fluid volume flux.

If it is assumed that these actuators deform these regions uniformly, that the volume of the jellyfish body remains constant, and that the velar flap itself does not deform in length then we can determine the rate of change of the cavity volume in terms of the strain rates $\dot{\epsilon}_1$, applied at markers ② and ③ in figure 7, and $\dot{\epsilon}_2$, applied at marker ① in figure 7

$$
\dot{\Omega} = -\dot{\epsilon}_1 \int_0^{s_1} r_\sigma^2 \left(\frac{\partial z_\sigma}{\partial s} + \frac{\partial r_\sigma}{\partial s} \right) \mathrm{d}s
$$
$$
- \frac{\pi \dot{\epsilon}_2}{2} \left(\frac{\dot{\epsilon}_2 \left(2 r_\sigma (s_1) - \dot{\epsilon}_2 \right)}{\sqrt{l_f^2 - \dot{\epsilon}_2^2}} + \sqrt{l_f^2 - \dot{\epsilon}_2^2} \right).
$$
(4)

In this equation r_σ and z_σ are the radial and axial positions of a point on the inner cavity surface which is at a distance, s along the surface, s_1 is the distance along the cavity surface to the velar flap joint and l_f is the length of the velar flap. It should be noted here that the volume flux is a function of both the strain rates at the two actuator locations as well as the current shape of the cavity surface. This should be expected as a body with a larger radial extent will expel more volume due to the body contraction associated with a given strain in body thickness, but it also means that the controller must have some knowledge of the current body shape in order to drive actuator strain required for the desired volume flux. For many simple robots an exact knowledge of the current shape may not be known. In such cases we can trim the flux-strain dynamics about the initial shape of the soft body, so that the integral term, $r_\sigma(s_1)$, and l_f in (4) all become constants that can be calculated from the initial shape, and volume flux is given purely as a function of actuator strains. The accuracy of such an approximation will decrease with large scale deformations, but should be reasonable given small deformations in shape.

The volume flux of *Sarsia tubulosa* during the jetting cycle is approximated from the two characteristic strains, ϵ_1 and ϵ_2, equating the shape of the body to its initial shape at all times. Figure 8(b) shows the volume flux computed by this approximation compared with the actual volume flux during the jetting cycle. It can be seen that the approximation is very close to the actual flux at the beginning of the cycle, as would be expected, but loses some accuracy during peak volume flux. However, throughout the entire cycle the error in

the approximation never gets larger than 15% of the actual volume flux. From a feedback controller standpoint this should be considered an acceptable approximation, since small errors in the predicted actuation dynamics can be corrected for in the feedback mechanism.

4. Epidermal-line inspired jetting feedback control mechanism

Previous sections examined volume flux programs that are beneficial to propulsive efficiency, indicating that impulsive volume flux programs minimize required energy for multiple cavity geometries. Though this optimal program may change slightly for different cavity geometries, we assume that there is some known, optimal, desired volume flux program $\dot{\Omega}$, which can be related to required body deformations (controls) and actuator strains. It is also imperative that the robot knows what deformations are actually being generated in real time, so that corrective actions can be taken when the jet volume flux strays from the desired programs. Here, we define a control law for a soft robot with a geometry and actuator configuration as presented in the previous section and introduce an algorithm for calculating jet flux parameters from internal pressure sensors inspired by the epidermal line of cephalopods.

The simple single parameter thruster illustrated in figure 2 has been outfitted with a linear potentiometer measuring real-time plunger deflection in experimental studies [20, 21, 23, 24]. If $h(t)$ is the internal height of this thruster's cavity, then a proportional derivative algorithm can be easily implemented to provide the control signal, u, for the linear actuator driving motion

$$
u(t) = k_p \left(\dot{\Omega}_d - \pi R_p^2 \dot{h} \right) + k_d \left(\ddot{\Omega}_d - \pi R_p^2 \ddot{h} \right) \quad (5)
$$

Here k_p and k_d are the proportional and derivative control gains, respectively, $\dot{\Omega}_d$ and $\ddot{\Omega}_d$ are the desired volume flux and desired rate of change of volume flux, respectively, and R_p is the radius of the flat plunger plate. This is in fact the control algorithm implemented in [24] to generate desired volume flux programs. This implementation works well in this case because h can be easily determined from a potentiometer which is rigidly attached to the back of the plunger.

For the case of a jellyfish-shaped soft robot, a similar proportional derivative control law can be created leveraging the relationship between actuator strain and volume flux (4), linearized about the initial body shape. Just like the previous control law, the error between desired volume flux and actual volume flux is used to generate the control signals, hence the controller must have some way of determining the actual volume flow rate at any given time. The flexible robot body results in complications in this regard, since without rigid joints (and motor encoders or

potentiometers) it is difficult to determine the exact magnitude of the deformation. Here again we draw inspiration from the sensory systems of marine invertebrates to generate an appropriate feedback mechanism.

Cephalopods have a sensory system known as the epidermal-line, which is functionally very similar to the lateral-line sensory system in fish [9, 10]. Much more research has been done on the fish lateral line, showing that the system is largely responsible for fish schooling [40], rheotaxis [4], and aids in obstacle detection when other senses are limited [41]. Superficial neuromasts on the body surface respond to the shear stress or the net velocity of the flow, whereas subdermal canal neuromasts respond to the pressure gradient or the net acceleration [12, 25, 26]. Some researchers have attempted to mimic the sensing capabilities of lateral line canal neuromasts with arrays of pressure sensors on robotic platforms [14, 43, 54, 62]. Although research on the epidermal line of cephalopods has been more limited, it has been observed that there are two lines of the system which extend along the funnel of cephalopods [30]. Furthermore, the broad band of ciliated cells on squid funnel as opposed to thin lines of octopus funnel [29, 30, 49] is likely due to the increased role jetting plays in squid locomotion, suggesting that the pressure distribution during jetting may serve as a good source of feedback for jet control. In fact, there is strong evidence that pressure varies greatly with the different mechanisms of thrust generation (i.e. different sources of vorticity generation).

Since there are no internal structures associated with the vorticity flux terms, the internal pressure due to this mechanism of circulation growth can be considered mostly uniform throughout the cavity. Certainly the half-sink flow exists within the cavity whenever the jet flow is present, but the circulation and pressure dynamics due to this internal flow structure are added separately. As such, a large degree of non-uniformity in the internal cavity pressure is indicative of a relatively high contribution from the half-sink circulation terms to the internal pressure. As an example, figure 9 shows the internal cavity pressure distribution at three characteristic moments throughout the jellyfish jetting cycle. In the first instance, figure 9(a), the jetting cycle has just started, so there is a large pressure associated with the fluid acceleration/half-sink circulation, and a limited pressure due to vorticity flux. At this time the pressure distribution is highly non-uniform with a large peak towards the outward radial edge of the cavity. In the second instance, figure 9(b), there is negligible jet acceleration and the internal pressure is dominated by the vorticity flux terms, resulting in the nearly uniform pressure distribution. In the third instance, figure 9(c), the fluid has begun to decelerate towards the end of the jetting cycle. Again the half-sink flow structure makes a large variation in internal pressure, but in this case the fluid deceleration acts in opposition to the flux of vorticity

and the pressure profile dips negative before reaching a peak closer towards the velar flap.

If several soft pressure sensors are placed internal to the cavity, similar to epidermal lines in cephalopod funnels, then the measured pressure distribution could be used as a feedback mechanism to drive corrective body deformations. The reference pressure is the sum of contributions from terms that scale with volume flux and terms that scale with the rate of volume flux, whereas the non-uniformity in pressure distribution is only due to the terms which scale with the rate of change of volume flux. We, therefore, surmise that the ratio of area under the non-uniform part of the pressure distribution $A_u(t)$ to reference pressure area $A_r(t)$ (see figure 10(a)) is proportional to the ratio of acceleration pressure terms to reference pressure

$$\frac{A_u}{A_r} - C_3 \propto \frac{C_2 \left| \ddot{\Omega} \right|}{C_1 \dot{\Omega}^2 + C_2 \ddot{\Omega}}. \tag{6}$$
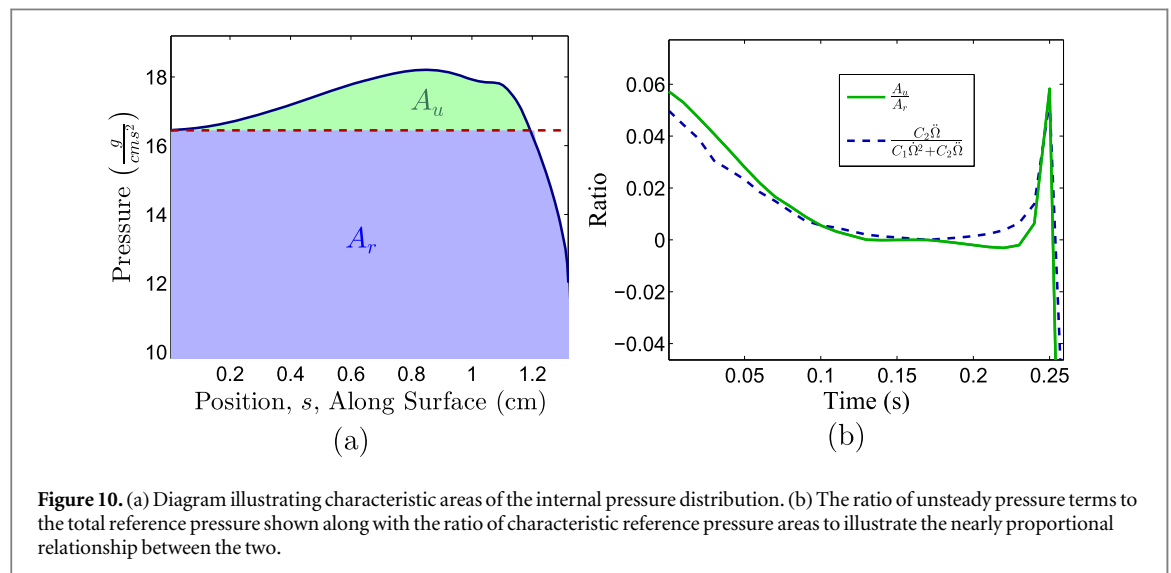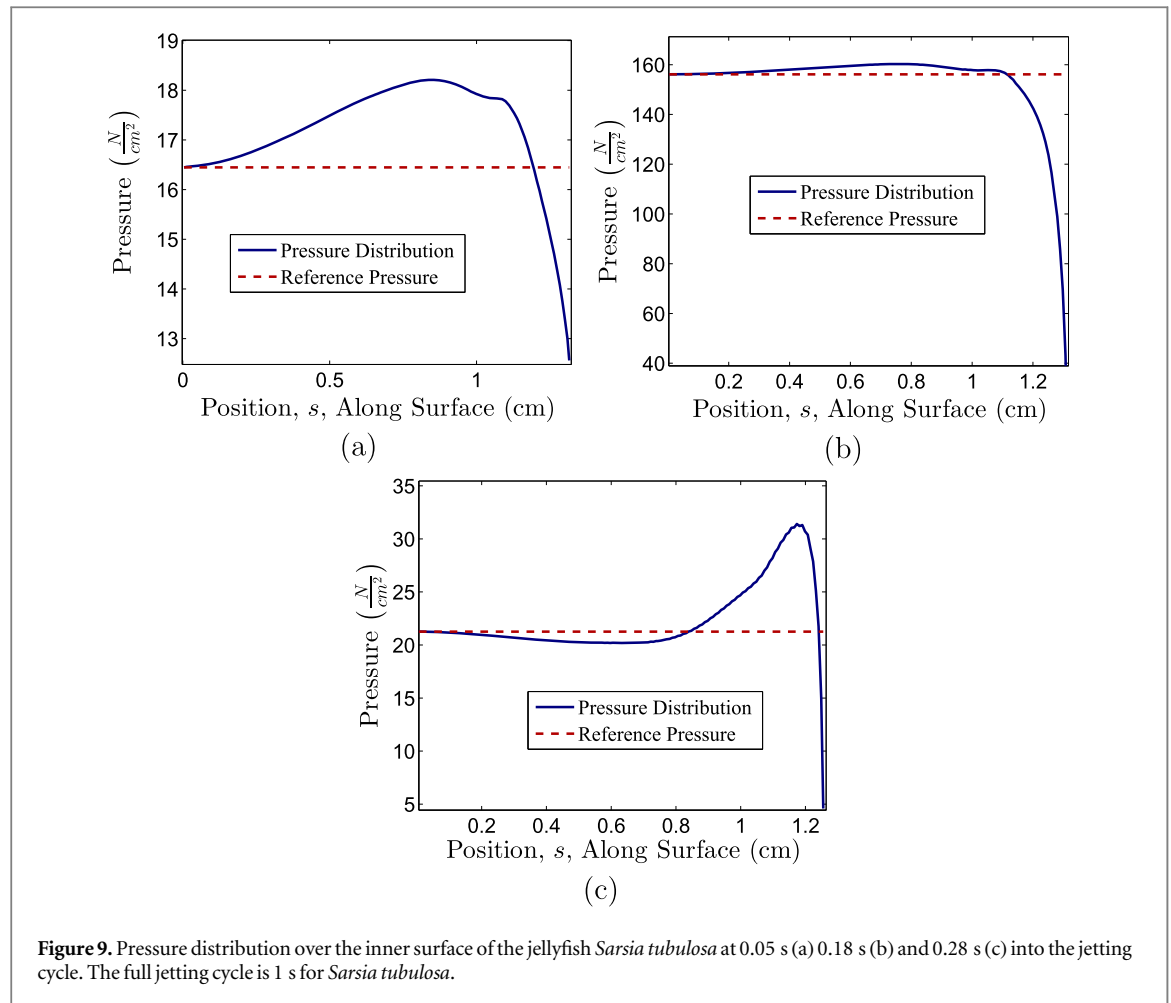
The term C_3 is to account for the fact that when the effect of the half-sink (acceleration) pressure terms become negligible there remains a degree of non-uniformity in the pressure distribution (i.e. the simplification that pressure distribution due to vorticity flux alone is uniform is not completely accurate). The coefficient C_3 must be calibrated in the laboratory prior to operation by measuring the ratio of A_u to A_r when $\ddot{\Omega} = 0$, and C_1 and C_2 are constants described in section 2.

The proportionality described in (6) is actually quite valid for the majority of the jetting phase, as can be seen in figure 10(b), where both ratios are shown with respect to time. The direction (sign) of $\ddot{\Omega}$ can also be determined from the pressure distribution since the pressure distribution will only drop below the reference pressure at any point if $\ddot{\Omega} < 0$. We denote this sign by $s_{\ddot{\Omega}}$, which is -1 when the jet flow is accelerating and $+1$ otherwise. Combining (2) and (6) allows us to determine the volume flux and rate of volume flux from the characteristic areas of the pressure distribution

$$\dot{\Omega} = \frac{1}{C1} \left[\frac{-P_b \left(\frac{A_u}{A_r} - C_4 + s_{\ddot{\Omega}} C_5 \right)}{\left(\frac{A_u}{A_r} - C_4 \right) \left(\frac{1}{C_2} - 1 \right) - s_{\ddot{\Omega}} C_5} \right]^{1/2}, \tag{7}$$

where C_4 is the constant of proportionality of (6), given a body-shape similar to *Sarsia tubulosa* $C_4 = 0.05$. The accuracy of this method at predicting volume flux during jetting is shown in figure 11. Here, it can be seen that the instantaneous volume flux can be estimated fairly well by determining the non-uniformity of the internal pressure profile.

With this information the control loop for the soft robot can be closed. The desired volume flux, $\dot{\Omega}_d$, is a given impulsive velocity program which along with the actual volume flux determined from the pressure sensor data (7) can be placed into the soft robot control law

Figure 9. Pressure distribution over the inner surface of the jellyfish *Sarsia tubulosa* at 0.05 s (a) 0.18 s (b) and 0.28 s (c) into the jetting cycle. The full jetting cycle is 1 s for *Sarsia tubulosa*.

Figure 10. (a) Diagram illustrating characteristic areas of the internal pressure distribution. (b) The ratio of unsteady pressure terms to the total reference pressure shown along with the ratio of characteristic reference pressure areas to illustrate the nearly proportional relationship between the two.

to generate appropriate control signals for the soft-actuators. It should be noted here that the coefficients C_4 and C_5 are specific to the *Sarsia tubulosa* body shape and must be determined by fitting the model to the actual pressure dynamics; however, the general underlying principle that non-uniformity in internal pressure during jetting corresponds to pressure from half-sink (accelerating flow) circulation dynamics is valid for any

flexible cavity geometry. Though the coefficients will need to be reevaluated for any alternative body shape, the methodology remains the same.

5. Conclusion

This paper provides analysis of several aspects of design specific to marine-invertebrate-inspired, underwater,
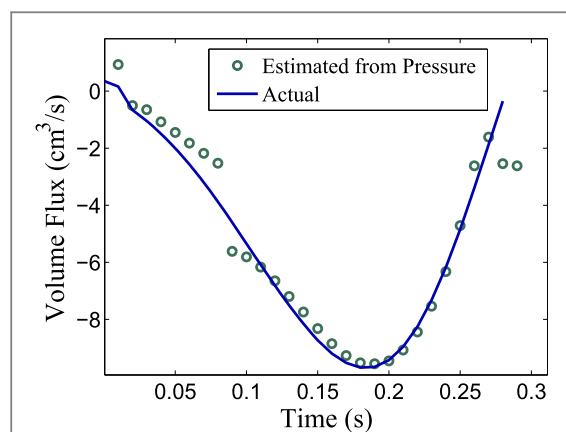
Figure 11. Volume flux of the propulsive jet is depicted along with the volume flux approximated by quantifying the relative non-uniformity of the internal pressure profile and relating it back to the pressure dynamics according to (7).

soft robots. The pressure dynamics inside a flexible cavity are described as they relate to the volume flux coming out of the cavity as well as the rate of change of that volume flux. As a result, it is shown that impulsive velocity programs minimize the energy required to drive fluid motion for certain cavity geometries, and it is assumed that any given cavity geometry has an optimal desired volume flux program (often impulsive) that should be achieved to increase efficiency. Next, the deformation of a hypothetical soft robot with the same body shape as the jellyfish *Sarsia tubulosa* is defined using a finite number of actuators. Motivation for actuator placement on the soft robot is driven here by actual deformations observed in that specific species of jellyfish, and a general technique is described to identify possible actuator locations from biological locomotion utilizing motion primitive analysis. Finally, a theoretical sensory feedback mechanism, inspired by the epidermal-line of cephalopods, is derived that allows the volume flux and flux rate to be determined from the pressure distribution inside the cavity. It is shown that shape of the pressure distribution inside the swimming jellyfish is highly indicative of the extent to which unsteady (rate of volume flux) terms affect the propulsive force. Furthermore, the exact quantification of this pressure distribution non-uniformity allows for high fidelity determining of volume flux and volume flux rate of the swimming jellyfish cavity, used as a model for the hypothetical soft robot body.

Acknowledgments

References

[1] Alben S, Witt C, Baker T V, Anderson E and Lauder G V 2012 Dynamics of freely swimming flexible foils *Phys. Fluids* **24** 051091

[2] Anderson E J and DeMont E 2000 The mechanics of locomotion in the squid *Loligo pealei*: locomotory function and unsteady hydrodynamics of the jet and intramantle pressure *J. Exp. Biol.* **203** 2851–63

[3] Anderson J M and Chhabra N K 2002 Maneuvering and stability performance of a robotic tuna *Integrative Comparative Biol.* **42** 118–26

[4] Baker C F and Montgomery J C 1999 The sensory basis of rheotaxis in the blind mexican cave fish, Astyanax fasciatus *J. Comp. Physiol.* **184** 519–27

[5] Barrett D S, Triantafyllou M S, Yue D K P, Grosenbaugh M A and Wolfgang M J 1999 Drag reduction in fish-like locomotion *J. Fluid Mech.* **392** 183–212

[6] Bartol I K, Krueger P S, Stewart W J and Thompson J T 2009 Hydrodynamics of pulsed jetting in juvenile and adult brief squid Lolliguncula brevis: evidence of multiple jet 'modes' and their implications for propulsive efficiency *J. Exp. Biol.* 1189–903

[7] Bartol I K, Krueger P S, Thompson J T and Stewart W J 2008 Swimming dynamics and propulsive efficiency of squids throughout ontogeny *Integrative Comparative Biol.* **48** 1–4

[8] Berman S M 1994 A bivariate Markov process with diffusion and discrete components *Commun. Stat.: Stoch. Models* **20** 271–308

[9] Budelmann B U and Bleckmann H 1988 A lateral line analogue in cephalopods: water waves generate microphonic potentials, in the epidermal head lines of sepia and lolliguncula *J. Comp. Physiol.* A **164** 1–5

[10] Budelmann B U, Riese U and Bleckmann H 1991 Structure, function, biological significance of the cuttlefish 'lateral lines' *The Cuttlefish: Acta I. Int. Symp. Cuttlefish Sepia* ed E Boucaud-Camou pp 201–9

[11] Clark R P and Smits A J 2006 Thrust production and wake structure of a batoid-inspired oscillating fin *J. Fluid Mech.* **562** 415–29

[12] Coombs S, Braun C B and Donovan B 2001 The orienting response of lake Michigan mottled sculpin is mediated by canal neuromasts *J. Exp. Biol.* **204** 337–48

[13] Dewey P A, Boschitsch B M, Moored K W, Stone H A and Smits A J 2013 Scaling laws for the thrust production of flexible pitching panels *J. Fluid Mech.* **732** 29–46

[14] Fernandez V I, Maertens A, Yaul F M, Dahl J, Lang J H and Triantafyllou M S 2011 Lateral-line-inspired sensor arrays for navigation and object identification *Mar. Technol. Soc. J.* **45** 130–46

[15] Ferreira de Sousa P J S A and Allen J J 2011 Thrust efficiency of harmonically oscillating flexible flat plates *J. Fluid Mech.* **674** 43–66

[16] Gibb A, Jayne B C and Lauder G V 1994 Kinematics of pectoral fin locomotion in the bluegill sunfish *Lepomis machrochirus J. Exp. Biol.* **189** 133–61

[17] Gosline J M and Shadwick R E 1983 The role of elastic energy-storage mechanisms in swimming — an analysis of mantle elasticity in escape jetting in the squid Loligo-Opalescens *Can. J. Zoology* **61** 1421–31

[18] Kato N 1998 Locomotion by mechanical pectoral fins *J. Mar. Sci. Technol.* **3** 113–21

[19] Krieg M, Klein P, Hodgkinson R and Mohseni K 2011 A hybrid class underwater vehicle: bioinspired propulsion, embedded system, and acoustic communication and localization system *Mar. Technol. Soc. J.: Spec. Ed. Biomimetics Mar. Technol.* **45** 153–64

[20] Krieg M and Mohseni K 2008 Thrust characterization of pulsatile vortex ring generators for locomotion of underwater robots *IEEE J. Ocean. Eng.* **33** 123–32

[21] Krieg M and Mohseni K 2010 Dynamic modeling and control of biologically inspired vortex ring thrusters for underwater robot locomotion *IEEE Trans. Robot.* **26** 542–54

[22] Krieg M and Mohseni K 2012 New perspectives on collagen fibers in the squid mantle *J. Morphology* **273** 586–95

[23] Krieg M and Mohseni K 2013 Modeling circulation, impulse and kinetic energy of starting jets with non-zero radial velocity *J. Fluid Mech.* **719** 488–526

[24] Krieg M and Mohseni K 2015 Pressure and work analysis of unsteady, deformable, axisymmetric, jet producing cavity-bodies *J. Fluid Mech.* **769** 337–68

[25] Kroese A B A, Van der Zalm J M and Van den Bercken J 1978 Frequency response of the lateral-line organ of Xenopus laevis *Pflügers Arch.* **375** 167–75

[26] Kroese A B A and Schellart N A M 1992 Velocity- and acceleration-sensitive units in the trunk lateral line of the canal *J. Neurophysiol.* **68** 2212–21

[27] Krueger P S 2005 An over-pressure correction to the slug model for vortex ring circulation *J. Fluid Mech.* **545** 427–43

[28] Lauder G V and Jayne B C 1996 Pectoral fin locomotion in fishes: testing drag-based models using three-dimensional kinematics *Integrative Comparative Zoology* **36** 567–81

[29] Lenz S 1997 Cilia in the epidermis of late embryonic stages and paralarvae of *Octopus vulgaris* (mollusca: Cephalopoda) *Vie Milieu* **47** 143–7

[30] Lenz S, Sundermann G and Fioroni P 1995 The epidermal lines of *Octopus vulgaris* Lamarck, 1798, and *Sepiola affinis* Naef, 1912 (mollusca: Cephalopoda), at hatching state *Zoologischer Anz.* **234** 145–57

[31] Lighthill M J 1969 Hydromechanics of aquatic animal propulsion *Annu. Rev. Fluid Mech.* **1** 413–46

[32] Lighthill M J 1970 Aquatic animal propulsion of high hydrodynamical efficiency *J. Fluid Mech.* **44** 265–301

[33] Lipinski D and Mohseni K 2009 Flow structures and fluid transport for the hydromedusae *Sarsia tubulosa* and *Aequorea victoria J. Exp. Biol.* **212** 2436–47

[34] Macgillivray P, Anderson E J, Wright G M and DeMont M E 1999 Structure and mechanics of the squid mantle *J. Exp. Biol.* **202** 683–95

[35] Mohseni K 2004 Pulsatile jets for unmanned underwater maneuvering *3rd AIAA Unmanned Unlimited Technical Conf., Workshop and Exhibit* (*Chicago, Illinois, 20–23 September 2004*) 2004–6386

[36] Moored K W, Dewey P A, Leftwich M C, Bart-Smith H and Smits A J 2011 Bioinspired propulsion mechanisms based on manta ray locomotion *Mar. Technol. Soc. J.* **45** 110–8

[37] Moored K W, Fish F E, Kemp T H and Bart-Smith H 2011 Batoid fishes: inspiration for the next generation of underwater robots *Mar. Technol. Soc. J.* **45** 99–109

[38] Moslemi A A and Krueger P S 2010 Propulsive efficiency of a biomorphic pulsed-jet vehicle *Bioinspiration Biomimetics* **5** 036003

[39] Moslemi A A and Krueger P S 2011 The effect of reynolds number on the propulsive efficiency of a biomorphic pulsed jet underwater vehicle *Bioinspiration Biomimetics* **6** 026001

[40] Partridge B L and Pitcher T J 1980 The sensory basis of fish schools: relative roles of lateral line and vision *J. Comp. Phys.* **135** 315–25

[41] Patton P, Windsor S and Coombs S 2010 Active wall following by Mexican blind cavefish (Astyanax mexicanus) *J. Comp. Physiol.* A **196** 853–67

[42] Quinn D B, Lauder G V and Smits A J 2014 Scaling the propulsive performance of heaving flexible panels *J. Fluid Mech.* **738** 250–67

[43] Ren Z and Mohseni K 2012 A model of the lateral line of fish for vortex sensing *Bioinspiration Biomimetics* **7** 036016

[44] Robert C and Casella G 2004 *Monte Carlo Statistical Methods* (New York: Springer)

[45] Sahin M and Mohseni K 2009 An arbitrary Lagrangian–Eulerian formulation for the numerical simulation of flow patterns generated by the hydromedusa *Aequorea victoria J. Comp. Phys.* **228** 4588–605

[46] Sahin M, Mohseni K and Colins S 2009 The numerical comparison of flow patterns and propulsive performances for the hydromedusae *Sarsia tubulosa* and *Aequorea victoria J. Exp. Biol.* **212** 2656–67

[47] Satterlie R A 2002 Neuronal control of locomotion in hydrozoan medusae: a comparative story *Can. J. Zoology* **80** 1654–69

[48] Serchi F G, Arienti A and Laschi C 2013 Biomimetic vortex propulsion: toward the new paradigm of soft unmanned underwater vehicles *IEEE/ASME Trans. Mechatronics* **18** 484–93

[49] Shigeno S, Kidokoro H, Goto T, Tsuchiya K and Segawa S 2000 Early ontogeny of the Japanese common squid *Todarodes pacificus* (Cephalopoda, Ommastrephidae) with special reference to its characteristic morphology and ecological significance *Zoological Sci.* **18** 1011–26

[50] Sledge I J, Krieg M, Lipinski D and Mohseni K 2015 Identifying and modeling motion primitives for the hydromedusae *Sarsia tubulosa* and *Aequorea victoria Bioinspiration Biomimetics* at press

[51] Tangorra J, Anquetil P, Fofonoff T, Chen A, del Zio M and Hunter I 2007 The application of conducting polymers to a biorobotic fin propulsor *Bioinspiration Biomimetics* **2** 6–17

[52] Triantafyllou M S, Hover F S, Techet A H and Yue D K P 2005 Review of hydrodynamic scaling laws in aquatic locomotion and fishlike swimming *Appl. Mech. Rev.* **58** 226–37

[53] Trivedi D, Rahn C D, Kier W M and Walker I D 2008 Soft robotics: biological inspiration , state of the art, and future research *Appl. Bion. Biomech.* **5** 99–117

[54] Venturelli R, Akanyeti O, Visentin F, Ježov J, Chambers L D, Toming G, Brown J, Kruusmaa M, Megill W M and Fiorini P 2012 Hydrodynamic pressure sensing with an artificial lateral line in steady and unsteady flows *Bioinspiration Biomimetics* **7** 036004

[55] Villanueva A, Smith C and Priya S 2011 A biomimetic robotic jellyfish (robojelly) actuated by shape memory alloy composite actuators *Bioinspiration Biomimetics* **6** 036004

[56] Villanueva A A, Joshi K B, Blottman J B and Priya S 2010 A bio-inspired shape memory alloy composite (bismac) actuator *Smart Mater. Struct.* **19** 025013

[57] Ward D V and Wainwright S A 1972 Locomotory aspects of squid mantle structure *J. Zoology* **167** 437–49

[58] Wolfgang M J, Anderson J M, Grosenbaugh M A, Yue D K P and Triantafyllou M S 1999 Near-body flow dynamics in swimming fish *J. Exp. Biol.* **202** 2303–27

[59] Wu T Y-T 1961 Swimming of a waving plate *J. Fluid Mech.* **10** 321–44

[60] Wu T Y-T 1971 Hydromechanics of swimming propulsion: I. Swimming of a two-dimensional flexible plate at variable forward speeds in an inviscid fluid *J. Fluid Mech.* **46** 337–55

[61] Wu T Y-T 1971 Hydromechanics of swimming propulsion: II. Some optimum shape problems *J. Fluid Mech.* **46** 521–44

[62] Xu Y and Mohseni K 2013 Bioinspired hydrodynamic force feedforward for autonomous underwater vehicle control *IEEE/ASME Trans. Mechatronics* **4** 1127–37